IBRACON Structures and Materials Journal
Revista IBRACON de Estruturas e Materiais
ISSN 1983-4195 ismj.org

ORIGINAL ARTICLE

Numerical modeling of a bolted beam-column connection subjected to cyclic loading

Modelagem numérica de uma ligação viga-pilar parafusada submetida a carregamento cíclico

Ygor Moriel Neuberger[a]
Daniel de Lima Araújo[b]
Marcelo de Araújo Ferreira[a]

[a]Universidade Federal de São Carlos – UFSCar, Departamento de Engenharia Civil, São Carlos, SP, Brasil
[b]Universidade Federal de Goiás – UFG, Escola de Engenharia Civil e Ambiental, Goiânia, GO, Brasil

Received 23 July 2025
Revised 13 October 2025
Accepted 27 October 2025

Abstract: In precast concrete systems, connections play a crucial role in ensuring structural continuity between elements and contributing to the overall stability of the structure. Among various types, semi-rigid bolted beam-to-column connections are commonly used to reduce on-site construction time. Additionally, they provide enhanced energy dissipation under seismic loading compared to cast-in-place connections. This study developed and validated a nonlinear numerical model in DIANA® software to simulate the behavior of a bolted beam-to-column connection under monotonic and cyclic loading. An analytical model was also proposed to estimate the secant stiffness of the connection. The numerical model was calibrated using experimental data available in the literature, showing a maximum error of 3% in predicting ultimate strength and 30% in energy dissipation capacity. Moreover, the model accurately represented the stiffness, cracking pattern, and global behavior of the connection. A parametric analysis was conducted to assess the influence of concrete strength, bolt diameter, and bolt steel grade on the connection performance. The comparison between cyclic and monotonic loading indicated low stiffness degradation up to the yielding of the bolts. The proposed analytical model yielded a stiffness ratio (numerical-to-analytical) of 1.00 with a coefficient of variation of 4.54%, confirming its applicability for estimating the stiffness of bolted connections.

Keywords: bolted beam-column connections, numerical modeling, analytical modeling, cyclic loading, secant stiffness.

Resumo: Nos sistemas pré-moldados, as ligações desempenham um papel fundamental ao garantir a continuidade estrutural entre os elementos e contribuir para a estabilidade global das estruturas. Dentre os diferentes tipos, as ligações viga-pilar aparafusadas semirrígidas são utilizadas quando se deseja reduzir o tempo de execução das ligações em obra. Além disso, elas proporcionam maior dissipação de energia quando submetidas à ação de sismos em relação às ligações realizadas com concretagem no local. Este estudo desenvolveu e validou um modelo numérico não linear no *software* DIANA® para reproduzir o comportamento de uma ligação viga-pilar parafusada sob carregamento monotônico e cíclico. Também foi proposto um modelo analítico para estimativa da rigidez secante da ligação. O modelo numérico foi calibrado a partir de dados experimentais disponíveis na literatura, apresentando erro máximo de 3% na previsão da resistência última e de 30% na capacidade de dissipação de energia pela ligação. Além disso, o modelo numérico mostrou-se preciso na representação da rigidez, fissuração e comportamento global da ligação. Uma análise paramétrica foi realizada para avaliar a influência da resistência do concreto, do diâmetro e do tipo de aço dos parafusos usados na ligação. A comparação entre carregamentos cíclicos e monotônicos revelou baixa degradação da rigidez da ligação até o escoamento dos parafusos. Já o modelo analítico proposto apresentou uma relação entre as rijezas numérica e analítica igual a 1,00 e coeficiente de variação de 4,54%, confirmando sua aplicabilidade para a estimativa da rigidez da ligação parafusada.

Palavras-chave: ligações viga-pilar parafusadas, modelagem numérica, modelagem analítica, carregamento cíclico, rigidez secante.

How to cite: Y. M. Neuberger, D. L. Araújo, and M. A. Ferreira, “Numerical modeling of a bolted beam-column connection subjected to cyclic loading” *Rev. IBRACON Estrut. Mater.*, vol. 18, no. 6, e18602, 2025, https://doi.org/10.1590/S1983-41952025000600002

Corresponding author: Ygor Moriel Neuberger. E-mail: ygor.neuberger@estudante.ufscar.br
Financial support: This work was supported by the Coordenação de Aperfeiçoamento de Pessoal de Nível Superior – Brasil (CAPES) – Finance Code 001, and the National Council for Scientific and Technological Development (CNPq) [grant number 404388/2021-3].
Conflict of interest: Nothing to declare.
Data Availability: The data that support the findings of this study are available from the corresponding author, Y. M. Neuberger, upon reasonable request.

1 INTRODUCTION

Precast structures differ from conventional structures by the industrialized manufacture of structural elements and the need for connections between components. Among the connections, beam-column connections are of great importance because, when semirigid, they give precast frames the capacity to transfer moments, ensuring that they function as a bracing frame and contributing to the overall stability of the structure. In this context, bolted connections have become popular due to their efficiency and rapid execution.

Connections are commonly classified as wet connections or dry connections. Wet connections require the use of concrete or mortar cast on site, which makes assembly laborious and prolongs installation time due to the need for formwork and curing of materials. On the other hand, dry connections use only welding, post-tensioning or screws, eliminating the need for casting on site [1]. Among dry connections, bolted connections stand out for their speed of execution and quality control, as well as requiring minimal intervention during assembly on site. In these connections, the bolts are mainly responsible for ensuring strength, ductility and energy dissipation, defining their structural behavior.

The performance of the precast concrete structures under seismic loads is critically dependent on the characteristics of the connections between precast members [2]–[6]. Ensuring adequate lateral resistance, energy dissipation, and minimum stiffness in these connections is essential for the seismic resilience of precast structures. The beam-column connections must be designed to withstand significant lateral forces without experiencing excessive deformation or failure. Precast frames can achieve a drift ratio up to 3.5%, which is larger than the maximum drift values allowed in most design codes around the world to avoid catastrophic failure [6]. However, for intermediate moment-resisting frames, a minimum drift ratio of 2.0% at the beam-column joints is enough [7], [8].

A beam-to-column connection with good energy dissipation capacity is needed to absorb energy input by seismic excitation, protecting other structural elements and ensuring satisfactory performance in the inelastic range [5], [9]. Emulative connections, which mimic cast-in-place construction, are designed to undergo flexural yielding and form ductile plastic hinges. Jointed connections concentrate nonlinear rotations at the ends of precast members, allowing the structure to undergo large lateral displacements with minimal tensile stresses in the concrete [4]. In areas with high seismic risk, precast concrete special moment-resisting frames should be used. In this case, the precast concrete frames have performance equivalent to the cast-in-place reinforced concrete frames when the relative energy dissipation ratio, β, measured in the third complete hysteresis curve at critical drift ratio, but not less than 3.5%, is greater than 1/8. The relative energy dissipation ratio is the area inside the lateral force-drift ratio loop divided by the area of the effective circumscribing parallelograms [4], [7], [8].

Minimum stiffness of beam-column connection is also necessary to control the lateral displacements and interstory drifts of the structure during seismic events. The initial stiffness of precast concrete frames is marginally lower than that of monolithic frames due to predefined gaps between prefabricated components. However, after yielding, precast connections could be slightly stiffer than monolithic connections. Moreover, precast concrete frames with additional bars could present the normalized stiffness degradation curves with decrease slower than that of monolithic frames [9]. This slower degradation is crucial for maintaining structural integrity during prolonged seismic activity. The stiffness of the third hysteresis curve at a drift ratio of 3.5% must be 0.05 times the initial stiffness or greater according to the ACI 374.2R-13 [4], [8].

Several authors, such as Aninthaneni et al. [10], [11], Aninthaneni and Dhakal [12], Zhang et al. [13] and Liu et al. [14], have carried out experimental research with semirigid bolted connections subjected to cyclic and monotonic loading. Various types of connection were used, from widening at the end of the beam, with bolts going through the column, to steel devices bolted at the end of the beam and fixed to the column. The tests showed good results in terms of strength, stiffness and ductility. However, testing these experimental models is expensive and requires specific laboratory equipment that is not always available.

In this scenario, numerical modeling using the finite element method (FEM) has emerged as an alternative for evaluating these connections, bringing savings and reliable results [15]. Authors such as Kallam and Bhanukumar [13], Zhang et al. [14], Ngo et al. [16] and Liu *et al.* [17] have numerically modeled bolted beam-column connections using the ABAQUS software® . The numerical results, when compared to the experimental models, showed good agreement in terms of stiffness and strength, with an error of less than 10% in the prediction of ultimate strength.

In addition to these studies, Nzabonimpa et al. [18] carried out tests on bolted beam-column connections with the aim of obtaining a typology that guaranteed a rigid connection. The authors used finite element modeling in the ABAQUS software® to design the thickness of the steel plate connecting the connection and to define the position and diameter of the bolts. After the tests, the authors compared the behavior of the experimental and numerical models and found good agreement. In this case, the numerical modeling helped in the design and decision-making process for the proposed connection type, highlighting another possible feature of this tool.

2 RESEARCH SIGNIFICANCE

Based on the results in the literature, the ABAQUS software®, combined with the CDP constitutive model, has been shown to be an effective tool for modeling bolted beam-column connections subjected to cyclic loading. However, there is still a lack of studies exploring other software and constitutive models. In this context, this work proposes the numerical modeling of the bolted beam-column connection tested by Liu et al. [14] using the DIANA software® . The aim is to identify the constitutive models and the most suitable parameters to accurately represent the behavior of this type of connection under reversible cyclic loading. In addition, by means of a parametric analysis, the study investigates the influence of the strength of the concrete, the diameter and the type of steel of the bolts used in the connection on the structural performance of the connection, with a focus on secant stiffness and energy dissipation. An analytical model for estimating the secant stiffness of the bolted beam-column connection before its yielding is proposed and validated using the results of the parametric analysis.

3 THREE-DIMENSIONAL NUMERICAL MODEL

3.1 Experimental Model

The experimental model developed by Liu et al. [14] consists of a column and a beam, both precast and connected at the end by bolts. Two specimens were tested, differing only in the diameter of the connecting bolts. Model S1 used bolts with a diameter (ϕ) of 24 mm, while model S2 used bolts with a diameter of 28 mm. Due to the consistency of the data reported and the type of loading applied, this study opted to use model S2 for numerical validation. It should be noted that up to a drift ratio of 3%, the maximum limit applied in the test, the S2 model demonstrated compliance with the performance criteria established by the ACI 374.2R-13 standard [8]. The relative energy dissipation index (β) obtained was 0.16, exceeding the minimum required value of 1/8 (approximately 0.125). In addition, the relative stiffness measured in the third hysteretic curve was 0.27, significantly higher than the minimum limit of 0.05 stipulated by the standard. These results indicate that the beam-column connection chosen has adequate capacity to dissipate energy and maintain stiffness under cyclic loading, and is therefore suitable for application in regions subject to seismic action.

The column, with a cross-section of 75 cm × 75 cm, was made from medium strength concrete. The beam, on the other hand, was made from lower strength concrete and had a section of 40 cm × 75 cm. The end of the beam was widened to 35 cm, matching the width of the column and allowing the metal connection bolts to be properly inserted. The design followed the "*strong column - weak beams*" philosophy, in which the column is designed to remain intact during seismic events, concentrating the strains on the beam. This makes it easier to replace the beam in the event of structural damage and maintains the integrity of the structure. The connection region was strengthened with steel plates and stiffeners.

The mechanical properties of the concretes used in the study were based on data adapted from Liu et al. [14]. For the lower strength concrete (beams), the cubic compressive strength was 28.48 ± 0.28 MPa, corresponding to a cylindrical compressive strength of 24.1 MPa. The medium strength concrete (column) presented a cubic compressive strength of 77.80 ± 0.46 MPa, with a corresponding cylindrical strength of 66.13 MPa. As the grout was not characterized, its compressive strength was assumed to be equal to that of the medium strength concrete, i.e., 66.13 MPa.

Strengthening reinforcements between 8 mm and 25 mm in diameter, 20 mm thick steel plates and 28 mm diameter bolts were used to make specimen S2. Tests to characterize the yield strength, ultimate strength, modulus of elasticity and elongation were carried out by the authors and results can be consulted at reference [14]. Figure 1 shows the details of the model.

The test was carried out using a servo-electro-hydraulic loading system with a capacity of ± 500 kN and a displacement stroke of ± 150 mm. The complete arrangement of the experiment is shown in Figure 2a. During the test, a vertical force was applied to the top of the column by means of a hydraulic actuator, maintaining a constant pressure ratio of 5% of the column's axial strength. After applying the vertical force, a symmetrical displacement with a low number of cycles was imposed on the beam, controlled by servo-electro-hydraulic actuators. The displacements at the end of the beam were applied according to the loading regime illustrated in Figure 2b. Analysis of the experimental results published by Liu et al. [14] showed a significant change in the behavior of the hysteresis curves from 110 mm of positive displacement. This change may be related to the interruption and restarting of the test, the breaking of the threads or the occurrence of large localized strains in the bolts. However, this aspect was not discussed by the authors in their analysis. Therefore, in this study, the loading regime was segmented into two stages, before and after this change in behavior, as shown in Figure 2b.

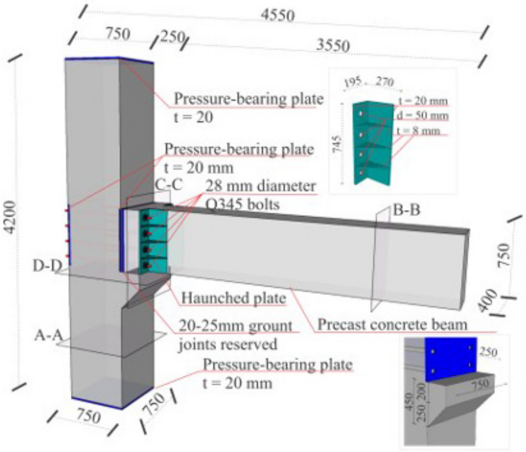

(a) Complete model.

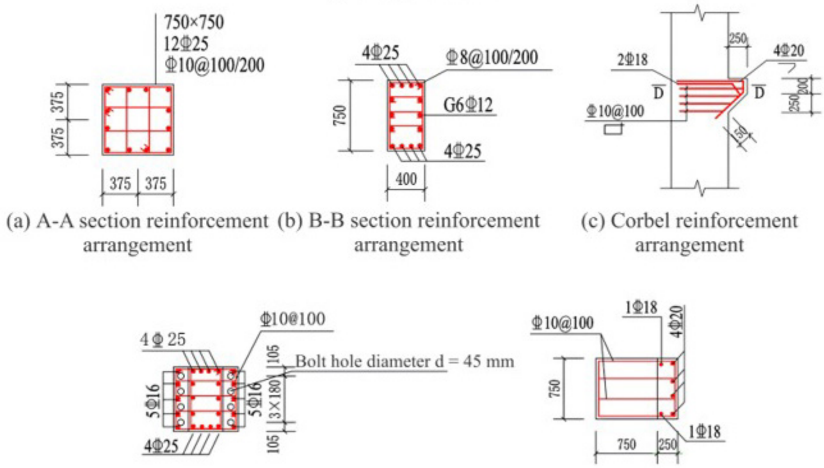

(a) A-A section reinforcement arrangement (b) B-B section reinforcement arrangement (c) Corbel reinforcement arrangement

(d) C-C section reinforcement arrangement (e) D-D section reinforcement arrangement

(b) Reinforcement detailing.

Figure 1. Experimental model. Adapted from Liu et al. [14].

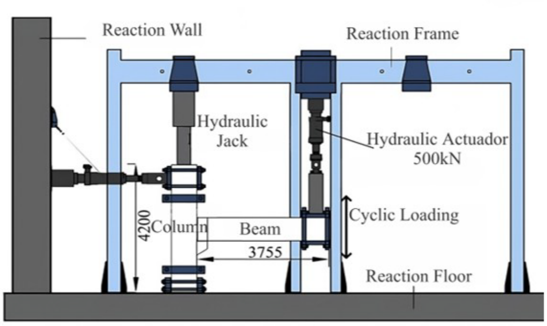

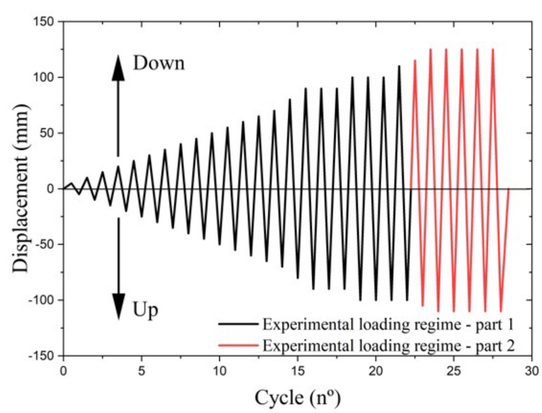

(a) Experimental setup. (b) Loading regime

Figure 2. Experimental setup and loading regime applied to the end of the beam for specimen S2. Adapted from Liu et al. [14].

3.2 The 3D Finite Element Model

The three-dimensional numerical model was developed using DIANA software® in version 10.2. Hexahedral linear interpolation finite elements with an average dimension of 50 mm (HX24L and PY15L) were used. This dimension was obtained from a mesh refinement analysis that sought to optimize the quality of the response and the processing time. Only half of the test specimen was modeled, using the principle of symmetry, which resulted in 35108 finite elements, according to the mesh that has been shown in Figure 3.

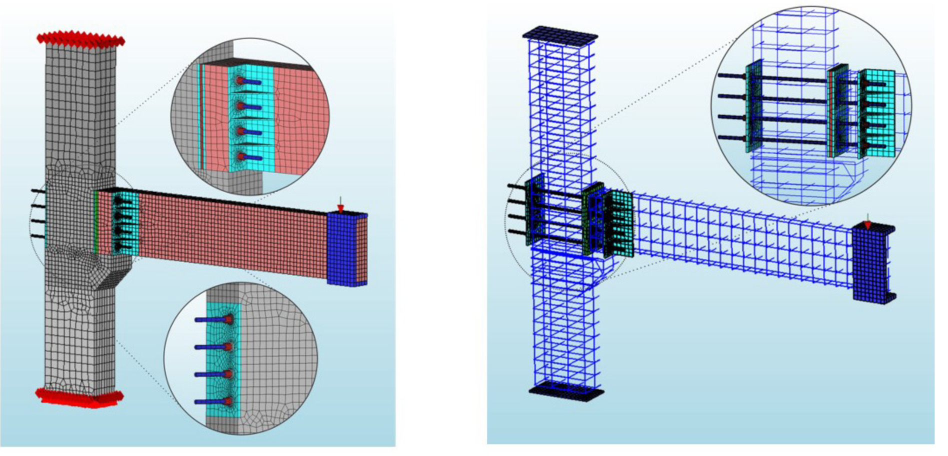

(a) Complete model. (b) Reinforcements and steel devices.

Figure 3. Finite element mesh of the beam-column connection.

The loading was applied in the DIANA software® using a phase analysis to simulate the loading applied during the test. Thus, in the first phase the column is initialized and stabilized with axial loading, in the second phase the beam is initialized and its own weight is applied, and finally the third phase includes the complete model, requested by imposing cyclic displacements at the end of the beam in increments of 2.5 mm.

The stiffness matrix solution was obtained using the BFGS (*quasi-newton*) secant method with the *line search* algorithm enabled. Convergence was obtained in terms of energy and displacement, with tolerances of 0.003.

3.2.1 Constitutive Models

3.2.1.1 Steel devices and reinforcements

The steel devices, such as loading plates, stiffeners, nuts, washers and bolts, were represented by the Von Mises plasticity model, using isotropic hardening. The use of kinematic hardening showed the same results as the model with isotropic hardening.

The beam and column strengthening reinforcements were represented using embedded reinforcement, available in the DIANA software®. These elements are not modeled as finite elements, but simulate the stiffening of the reinforcements in the solid elements around them. Perfect adhesion between the reinforcement and the concrete was assumed, and the behavior of the reinforcement was also simulated with the *Von Mises* plasticity model and isotropic hardening.

3.2.1.2 Concrete and grout

The concrete of the column was represented using the Total strain-based crack model, while the concrete of the beam and the grout filling the joint were represented using the Maekawa-Fukuura model. This model was developed to represent concrete structures subjected to cyclic loading [19] and is available in the software library. Table 1 presents the parameters used to define the constitutive models for both concrete types: column concrete properties are listed in the second column, and the beam (including the grout) properties are shown in the third column. It should be noted that the paper by Liu et al. [14] provided only the basic concrete properties (f_{cm}), which are not sufficient to fully define the Maekawa-Fukuura constitutive model. Therefore, the values listed in Table 1 were established in the present study based on the validation of the 3D finite element model against the experimental results reported by Liu et al. [14]. The results of the numerical model validation are presented in Section 4.

3.2.1.3 Interfaces

The beam-column connection tested by Liu et al. [14] has several joints, which were not characterized by the authors. Therefore, this research sought to determine the most suitable constitutive models for representing the joints present in the connection. Q24IF interface finite elements were used in four regions of the beam-column connection to represent the behavior observed in the experimental model. The interface elements were used between the corbel and the bottom face of the beam (Corbel interface), between the steel plate fixed to the column and the vertical face of the grout used to fill the joint between the beam and the column (Negative vertical interface and Positive vertical interface), and between the washers and the steel plates used to fix the tie bars (Washer-nut interface).

Table 1. Constitutive model and concrete properties of the material in DIANA software®.

Property	*Column*	*Beam and grout*
Class	*Concrete and Mansory*	*Concrete and Mansory*
Model	*Total strain-based crack model - Fixed*[c]	*Maekawa-fukuura concrete model*[c]
Linear Material Properties		
Modulus of Elasticity (E_c) [a, b]	$E_c = 21500\ (f_{cm}/10)^{1/3}$	-
Poisson's ratio (ν) [a]	$\nu = 0.2$	-
Strain at compressive strength	-	2.2 ‰[a]
Density (ρ) [a]	$\rho = 2500$ kg/m³	$\rho = 2500$ kg/m³
Tensile behavior		
Threshold angle between cracks	-	0.3927 rad[d]
Crack-reclosing option	-	Enabled
Tension softening	*Hordijk* [c]	*Hordijk* [c]
Damage based tensile strength reduction	-	No reduction, $R_f = 1$[d]
Tensile strength (f_{ct}) [a, b]	$f_{ct} = 0.3 f_{cm}^{2/3}$, $f_{cm} \leq 50$Mpa $f_{ct} = 2.12\ ln(1+0.1 f_{cm})$	$f_{ct} = 0.3 f_{cm}^{2/3}$, $fcm \leq 50$Mpa $f_{ct} = 2.12\ ln(1+0.1 f_{cm})$
Fracture energy [a, b]	$G_f = 73\ f_{ck}^{0.18}$ N/m	$G_f = 73\ f_{ck}^{0.18}$ N/m
Crack bandwidth specification	*Rots*	*Rots*
Compressive behavior		
Type of compressive behavior:	*Multi-linear diagram*	-
Compressive strength [b]	f_{cm} [b]	f_{cm} [b]
Stress-strain relation	*Lim and Ozbakkaloglu* [20]	-
Reduction due to lateral cracking	*No Reduction*	-
Lateral expansion effects due to poisson's ratio	*Selby and Vecchio* [c]	-
Shear behavior		
Shear retention function	*Constant* [c]	Contact density with decay [a]
Ultimate shear strain	-	0.05[e]
Power C for shear retention	-	0.4 [d]
Shear retention (β)	*0.01* [d]	*0.01* [d]
Reduction due to lateral cracking	*No Reduction* [d]	*No Reduction* [d]
Poisson's ratio reduction model	-	*No Reduction* [d]

[a] Recommendation of the *fib* Model Code 2010 [21], maintained after verification with the *fib* Model Code 2020 version [22], with a difference of bottom 5% for the concrete classes used. [b] For modeling, we adopted $f_{ck} = f_c = f_{cm}$. [c] Model available on DIANA® version 10.2. [d] DIANA Default® Version 10.2. [e] Adopted in this research.

The interface between the beam flange and the steel stiffener was also evaluated, but as it had no significant influence on the overall behavior of the connection, it was discarded from the model. As the connection was subject to positive and negative bending moments, it was necessary to assign different properties to the interface between the steel plate and the grout in order to correctly represent the stiffness of the connection when subjected to bending moment inversion. In Figure 4 the two interfaces have been shown, which were equal in height to half the height of the beam. The constitutive model adopted for the interfaces was discrete cracking, with brittle joint opening. The stiffness values of the interfaces are the result of this research and were obtained based on the experimental results of the beam-column connection and are presented in Table 2.

Table 2. Interface stiffnesses of the beam-column connection.

Material	N-z (N/mm^3)	S-x (N/mm^3)	S-y (N/mm^3)
Corbel interface	200	5	5
Negative vertical interface	0.5	0.5	0.5
Positive vertical interface	5	0.75	0.75
Washer-nut interface	225	5	5

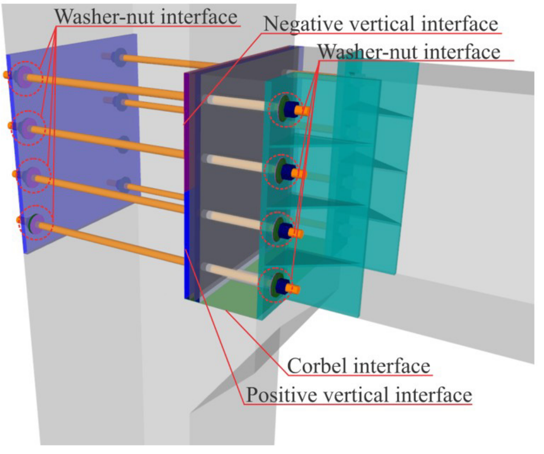

Figure 4. Defined interfaces between connection joints.

4 VALIDATION OF THE NUMERICAL MODEL

This section presents the results obtained using the numerical model, which are compared with the experimental data, including: skeleton curves, cyclic loading curves (force × displacement), energy dissipation and cracking pattern. It should be noted that the numerical model was able to accurately represent the behavior observed experimentally up to the limit of 110 mm displacement (drift rate 2.6%), corresponding to the first loading regime, as illustrated in Figure 2b. All the numerical analysis will be carried out up to this limit.

Figure 5 shows the skeleton curves obtained from the numerical model and the experimental model. This curve indicates the greatest strength obtained during cyclic loading for each value of displacement imposed on the connection. There was good agreement between the curves, both for positive displacements, i.e. negative bending moment in the connection, and for negative displacements, i.e. positive bending moment in the connection.

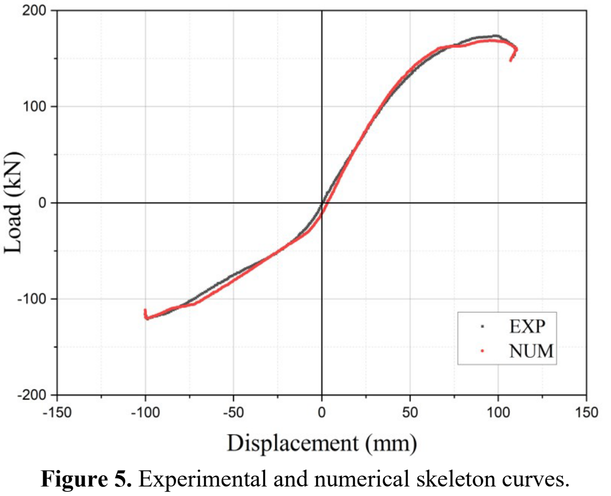

Figure 5. Experimental and numerical skeleton curves.

With a positive displacement of 100 mm, the maximum experimental force ($P_{max,exp}$) was 173.18 kN, while the maximum numerical force ($P_{max,num}$) was 168.81 kN for the same displacement, resulting in a $P_{max,num}/P_{max,exp}$ ratio of 0.97. For the negative displacement of 100 mm, the minimum experimental force ($P_{min,exp}$) of -122.77 kN was obtained, while the minimum numerical force ($P_{min,num}$) was -120.68 kN, resulting in a $P_{min,num}/P_{min,exp}$ ratio of 0.98. These results represent an error of only 3% of the numerical model in predicting the strength of the beam-column connection.

While the skeleton curve only shows the maximum force values in each displacement cycle, the cyclic force × displacement curve, which has been shown in Figure 6a, shows the evolution of the force over the entire loading history. An excellent hysteresis correlation is observed for positive displacements, i.e. negative bending moments in the connection. However, for negative displacements, i.e. positive bending moments in the connection, this behavior was not fully represented. This can be attributed to the gaps that appeared between washers and bolts in the experimental model when the loading was reversed, which were not fully represented in the numerical model using the interface element.

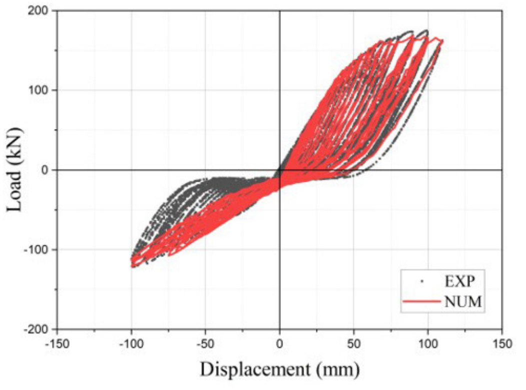

(a) Experimental and numerical hysteresis curves.

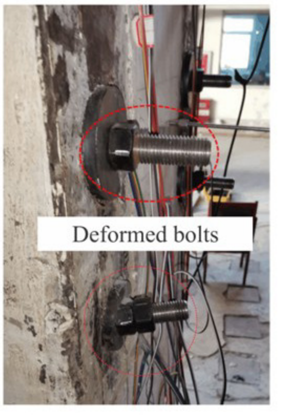

(b) Strains after rupture.

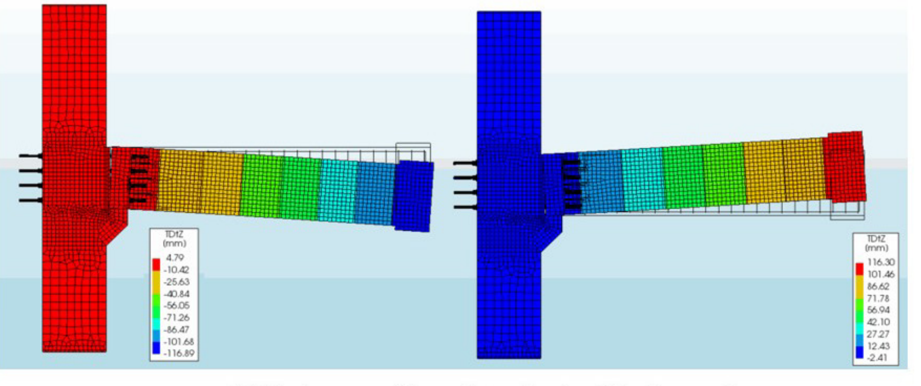

(c) Maximum positive and negative bond displacements.

Figure 6. Load-displacement curves and experimental and numerical behavior.

In addition, it can be seen in Figure 6b that there has been slippage between the nuts and the tie bars at the bottom of the connection, probably due to the strain on the threads of the bolt. Figure 6c has shown the maximum positive and negative displacements of the model, where it is possible to see the straightness of the bolts, even under large displacements. This type of plastic strain is particularly difficult to simulate accurately in the numerical model without the representation of the thread fillet or by an equivalent interface. As the paper by Liu et al. [14] did not provide parameters for the representation of this interface, the numerical model was developed assuming perfect adherence between the nuts and the tie bars. These authors carried out numerical modeling of the connection and also did not achieve adequate representation of the connection's hysteresis when subjected to a positive bending moment. Despite this limitation, the stiffness of the connection when subjected to a positive bending moment was adequately represented by the numerical model developed in this paper, as can be seen in the comparison between the experimental and numerical stiffness degradation curves shown in Figure 7.

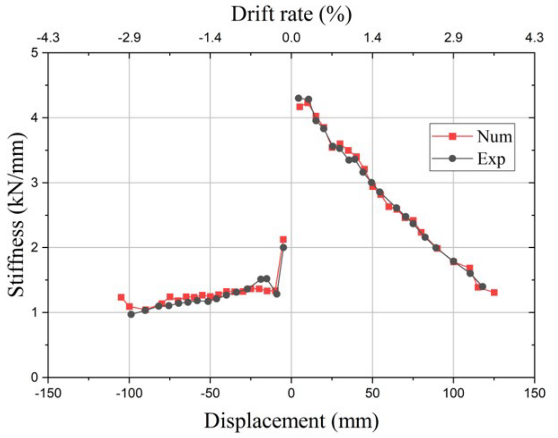

Figure 7. Stiffness degradation curves.

Table 3. Comparison between experimental and numerical energy dissipation.

Cycle	Experimental Hysteresis H_{exp} [kN-mm]	Numerical Hysteresis H_{num} [kN-mm]	H_{num}/H_{exp}
1º ± 90 mm	2829.3	3506.9	1.24
2º ± 90 mm	1488.8	1609.8	1.08
3º ± 90 mm	1156.7	1860.8	1.61
1º ± 100 mm	2456.3	3350.8	1.36
2º ± 100 mm	1520.4	1957.6	1.29
3º ± 100 mm	1530.1	1842.6	1.20

Table 3 shows the comparison between the dissipated energies, expressed by the area of the hysteresis loops, obtained in the last six loading cycles of the experimental and numerical models. It can be seen that although the numerical model did not accurately reproduce the hysteretic behavior under positive bending moment, as shown in Figure 6a, the values of dissipated energy were generally consistent with the experimental data. The average ratio between numerical and experimental hysteresis was 1.30, indicating a tendency for the numerical model to overestimate the energy dissipated, with values approximately 30% higher than those obtained experimentally.

Figure 8a and 8b show the crack pattern obtained in the numerical model, which is compared to the crack pattern in the paper by Liu et al. [14], which has been shown in Figure 8d. In both the experimental and numerical models, there is a predominance of vertical bending cracks at a distance of approximately 140 cm from the column face. In addition, there is a large number of cracks in the widening region of the beam, caused by shear resulting from the transfer of stresses between the longitudinal reinforcement and the bolts, which are eccentric. At the end of the test, significant damage was observed in the beam's concrete between the flange and the corbel, as illustrated in Figure 8c and 8e, a phenomenon that was also captured by the numerical model. In general, the numerical model was able to adequately represent the cracking observed in the experimental model.

4 PARAMETRIC ANALYSIS

A parametric analysis was carried out using the numerical model to evaluate the influence of the beam's concrete, the diameter of the bolts and the type of steel in the bolts on the behavior of the connection. Three values were chosen for the strength of the concrete: 24 MPa, 40MPa and 55MPa. The 24 MPa concrete is the same as that used by the reference [14], while the 40 MPa and 55 MPa concretes represent concretes with higher strengths and are commonly used in the precast concrete industry. The study also analyzed three different bolt diameters: 28 mm, 22 mm and 16 mm. The 28 mm bolted is the same as that used in the reference [14], while the 22 mm and 16 mm diameters represent commercial diameters with approximately 2/3 and 1/3 of the steel area, respectively. Finally, three different materials were also used for the bolts: the Q345 steel used in the reference [14] (with f_y = 436 MPa and f_u = 764 MPa), the standard CA-70 steel used in Brazil (with f_y = 700 MPa and f_u = 840 MPa) and a high strength SAE 10B38 grade 8.8 steel (with f_y = 834 MPa and f_u = 942 MPa), tested and characterized by Kodur et al. [23]. The parametric modeling resulted in 27 specimens which are represented in Figure 9.

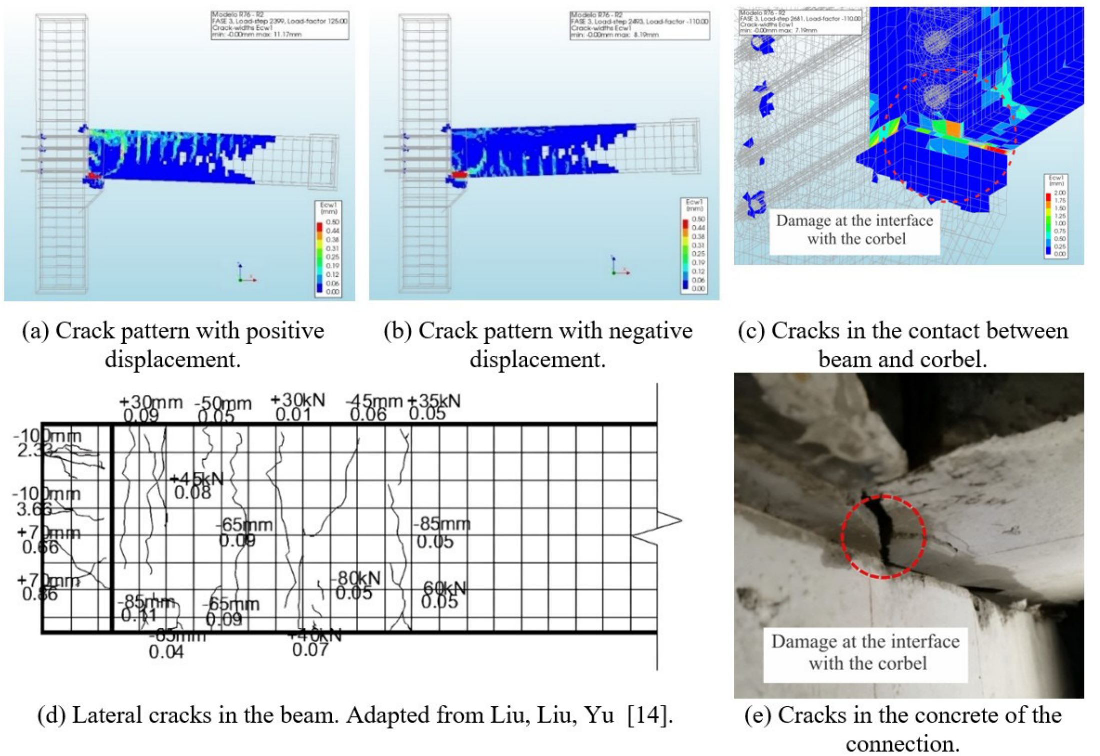

(a) Crack pattern with positive displacement.
(b) Crack pattern with negative displacement.
(c) Cracks in the contact between beam and corbel.
(d) Lateral cracks in the beam. Adapted from Liu, Liu, Yu [14].
(e) Cracks in the concrete of the connection.

Figure 8. Experimental and numerical comparison of the crack pattern.

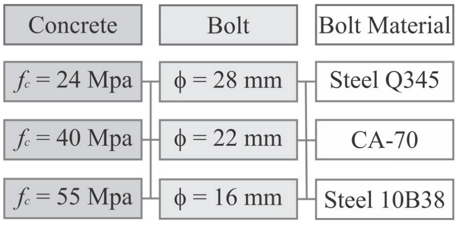

Figure 9. Schematic representation of parametric modeling.

The models were named after the strength of the concrete and the diameter and steel of the bolts, respectively. Thus, model C24_F28_Q345 represents 24 MPa concrete, with a bolt diameter of 28 mm and Q345 steel, which was the model tested in the reference [14] and used to calibrate the numerical model.

4.1 COMPARISON BETWEEN CYCLIC AND MONOTONIC LOADING

In order to assess the influence of the type of loading on the behavior of the connections, the parametric analysis models were subjected to both monotonic loading (up to a limit of 150 mm in each direction) and cyclic loading, according to the regime shown in part 1 of Figure 2b.

Figure 10 shows the force × displacement curves of two representative models: one with a lower reinforcement ratio (C55_F16_Q345, 16 mm bolts) and one with a higher ratio (C55_F28_Q345, 28 mm bolts). It can be seen that, for most displacements, the skeleton curve of cyclic loading coincides with that of monotonic loading, diverging only for higher displacements. This difference occurs after the flow of the first line of bolts, as shown in Figure 10 by the point P_y. This behavior suggests that, for most of the conditions analyzed, cyclic effects do not significantly alter the strength of the connection.

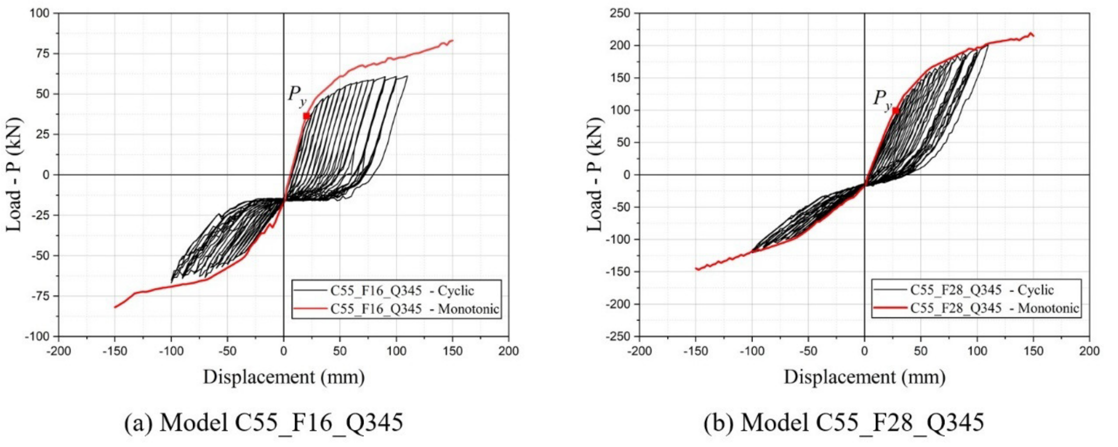

Figure 10. Comparison of strength between cyclic and monotonic loading.

Table 4 shows the strength values at the maximum positive and negative displacements. The ratio between the values obtained under cyclic and monotonic loading for the maximum positive displacement was 0.93, with a coefficient of variation (COV) of 7.15%. For the negative displacement, the ratio was 1.01, with a COV of 5.27%, indicating a low influence of cyclic loading in reducing the stiffness of the bond.

To evaluate the influence of the variables (bolt diameter, steel strength and concrete strength) on the stiffness ratio between cyclic and monotonic loading for the positive bending moment, a multiple linear regression was performed. The model was statistically significant ($F(3.23) = 24.609$, $p < 0.001$, $R^2 = 0.767$), explaining 76.7% of the variability of the dependent variable.

All the variables were significant predictors: bolt diameter ($\beta = 0.553$; $t = 5.442$; $p < 0.001$), steel strength ($\beta = 0.496$; $t = 4.885$; $p < 0.001$) and concrete strength ($\beta = 0.458$; $t = 4.512$; $p < 0.001$). Although the diameter of the bolts stood out as the variable with the greatest statistical influence on the variation of the stiffness ratio between the cyclic and monotonic loads for the positive bending moment, the standardized coefficients (β) of the strength of the steel and concrete showed very close values. This indicates that the three variables contribute similarly to explaining the observed behavior.

4.2 ENERGY DISSIPATION

Figure 11 shows the evolution of the accumulated energy dissipated by the models over the loading cycles. It can be seen that model C24_F28_10B38 dissipated the most energy, while model C55_F16_Q345 had the lowest accumulated values. The dissipation of energy over the cycles is associated with different mechanisms, such as yielding of the reinforcement, friction between structural components and, above all, the progressive degradation of the concrete.

In the numerical modeling adopted, the kinematic behavior of the steel was tested and showed little influence on the results obtained, strengthening the predominant contribution of concrete degradation to energy dissipation. Thus, in the models with a higher reinforcement ratio and high strength steel, greater accumulated dissipation was observed, probably related to the greater concentration of stresses and the consequent localized degradation of the concrete.

To investigate the influence of the variables analyzed on energy dissipation, a multiple linear regression was performed. The model showed statistical significance [$F(3.23) = 379.09$, $p < 0.001$] and explained 98% of the variability observed in dissipated energy ($R^2 = 0.98$). All the independent variables included were significant predictors: the diameter of the bolts showed the greatest effect on the dependent variable ($\beta = 0.907$; $t = 30.89$; $p < 0.001$), followed by the strength of the concrete, which showed an inverse relationship with energy dissipation ($\beta = -0.321$; $t = -10.94$; $p < 0.001$), suggesting that lower strength concretes provide greater energy dissipation. Steel strength, although also significant, exerted the smallest relative influence on the model ($\beta = 0.233$; $t = 7.953$; $p < 0.001$). These results strengthen the conclusion that reinforcement diameter is the main factor associated with energy dissipation in the models analyzed.

Based on the variables analyzed, it was possible to establish a relationship between accumulated energy dissipation and the mechanical reinforcement ratio (ω). Figure 12 shows the logarithmic regression curve fitted to the data, with determination coefficient $R^2 = 0.86$, indicating a good level of fit. This equation can be used to estimate energy dissipation in systems with mechanical rates varying between 0.025 and 0.40.

Table 4. Influence of the type of loading on the maximum loads for positive and negative displacements.

Model	Positive Displacement [a]			Negative Displacement [b]		
	Monotonic Load [kN]	Cyclic Load [kN]	Cyclic/ Monotonic	Monotonic Load [kN]	Cyclic Load [kN]	Cyclic/ Monotonic
C24_F28_Q345	191.4	170.7	0.89	-115.3	-124.4	1.08
C40_F28_Q345	203.9	186.4	0.91	-118.9	-126.0	1.06
C55_F28_Q345	203.1	200.9	0.99	-117.7	-120.6	1.03
C24_F22_Q345	133.3	114.4	0.86	-97.4	-98.4	1.01
C40_F22_Q345	127.9	117.9	0.92	-97.4	-97.1	1.00
C55_F22_Q345	137.8	124.8	0.91	-98.2	-107.0	1.09
C24_F16_Q345	67.5	55.4	0.82	-70.0	-62.4	0.89
C40_F16_Q345	73.6	60.6	0.82	-71.2	-68.0	0.95
C55_F16_Q345	73.6	61.2	0.83	-69.2	-65.0	0.94
C24_F28_CA-70	230.4	216.8	0.94	-136.0	-138.8	1.02
C40_F28_CA-70	233.8	242.4	1.04	-138.8	-137.4	0.99
C55_F28_CA-70	248.6	252.3	1.01	-138.7	-139.2	1.00
C24_F22_CA-70	181.1	153.5	0.85	-110.9	-108.5	0.98
C40_F22_CA-70	180.6	174.6	0.97	-116.8	-129.9	1.11
C55_F22_CA-70	187.7	182.9	0.97	-112.7	-112.0	0.99
C24_F16_CA-70	105.9	91.5	0.86	-84.3	-82.9	0.98
C40_F16_CA-70	107.1	95.4	0.89	-89.5	-86.8	0.97
C55_F16_CA-70	109.3	99.4	0.91	-85.6	-84.1	0.98
C24_F28_10B38	231.3	208.2	0.90	-137.8	-137.3	1.00
C40_F28_10B38	237.1	247.2	1.04	-141.0	-145.6	1.03
C55_F28_10B38	251.7	265.3	1.05	-142.1	-146.2	1.03
C24_F22_10B38	206.5	181.2	0.88	-118.3	-117.9	1.00
C40_F22_10B38	209.6	198.4	0.95	-120.7	-130.2	1.08
C55_F22_10B38	215.5	208.7	0.97	-123.2	-120.4	0.98
C24_F16_10B38	117.9	110.9	0.94	-88.3	-87.1	0.99
C40_F16_10B38	122.8	118.4	0.96	-91.0	-87.2	0.96
C55_F16_10B38	130.2	123.9	0.95	-92.6	-103.7	1.12
Média			0.93			1.01
D.P.			0.07			0.05
COV			7.15%			5.27%

[a] Corresponds to the maximum positive displacement of 110 mm. [b] Corresponds to the maximum negative displacement of -100 mm

The relative energy dissipation index (β) varied between 0.04 and 0.07, falling below the minimum of 1/8 established by the ACI 374.2R-13 [8] standard for use in Special Moment Frames in areas of high seismicity. Despite this, the values obtained are compatible with the application of the connection in regions of moderate earthquake, as long as it is included in systems classified as *Intermediate Moment Resisting Frames* (IMRF). The discrepancy between the experimental results and those obtained through numerical modeling can be attributed to the limitation of the *drift rate* considered. As shown in Table 3, the numerical model adequately represented the behavior of the connection up to a *drift rate of* 2.6%. For higher values, the model was unable to capture the observed behaviour, probably due to the occurrence of localized strains, such as those shown in Figure 6b, which are complex to reproduce computationally.

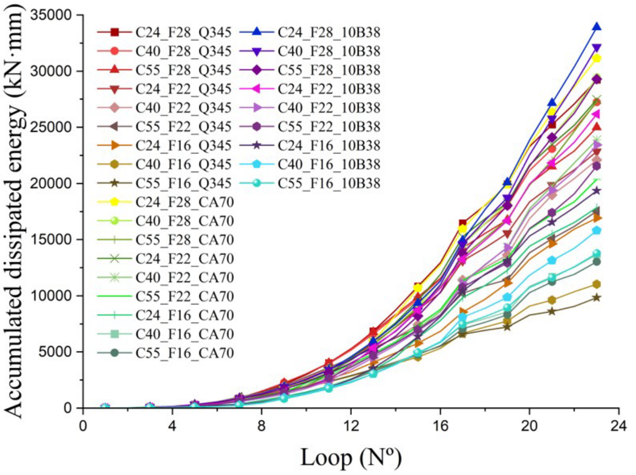

Figure 11. Accumulated dissipated energy under cyclic loading.

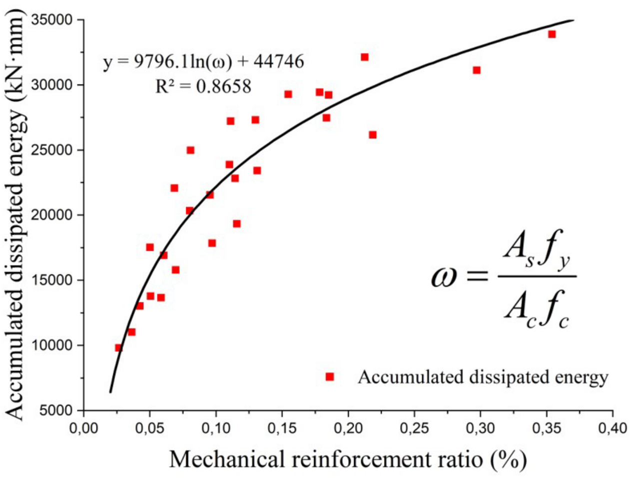

Figure 12. Relationship between accumulated dissipated energy and geometric reinforcement ratio - ω.

4.3 NEGATIVE STIFFNESS OF THE CONNECTION UNDER MONOTONIC LOADING

The secant stiffness of the connection can be defined by the ratio between the bending moment resisted by the connection (*M*) and its rotation (*θ*), as shown in Equation 1.

$$R = \frac{M}{\theta} \tag{1}$$

$$M = P\,L \tag{2}$$

The bending moment is determined by the Equation 2, where *P* is the force applied to the free end of the beam and *L* is the distance between the point of application of the force and the center of the corbel, considered to be 3.49 m.

The total displacement (δ_T) at the free end of a cantilever beam depends on two components: the deflection of the beam considered to be attached to the support (δ_1) and the rigid body rotation (*θL*), as shown in Figure 13. The rigid body rotation is directly linked to the rotation of the connection at the support. Therefore, the rotation of the connection can be calculated using Equation by subtracting the value of the displacement due to deflection from the total displacement and dividing the resulting displacement by the length of the overhanging section (*L*).

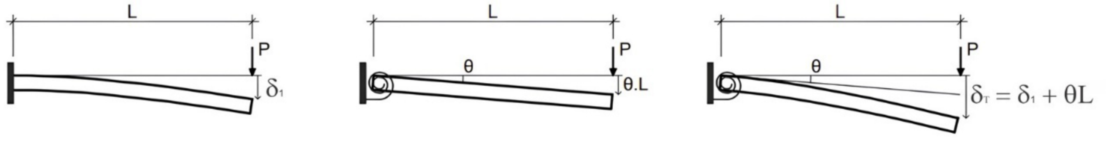

(a) Deflection. (b) Rigid body rotation. (c) Total displacement.

Figure 13. Composition of the displacement of a cantilever beam connected to a semirigid connection.

$$\theta = \frac{\delta_T - \delta_1}{L} \tag{3}$$

The deflection of the beam (δ_1) was calculated using Equation 4, where E_c is the modulus of elasticity of the concrete and I_{eq} is the equivalent inertia of the beam considering the cracking of the concrete, which was calculated using the expression proposed by Shaikh and Branson [24], according to Equation 7. This expression interpolates the values of the inertia of the uncracked concrete section (I_c) and the cracked inertia at stage II (I_{II}), according to the loading stage of the beam, which is evaluated by the ratio between the maximum bending moment along the beam (M) and the cracking moment of the beam cross-section (M_r).

The cracking moment of the beam was calculated using Equation 6 recommended in the ABNT NBR 6118 standard [25], where f_{ct} represents the tensile strength of the concrete and y_t is the distance between the geometric center of the section and the most tensile fiber, adopted as half the height for rectangular beams.

$$\delta_1 = \frac{PL}{3E_c I_{eq}} \tag{4}$$

$$I_{eq} = \left(\frac{M_r}{M}\right)^3 I_c + \left[1 - \left(\frac{M_r}{M}\right)^3\right] I_{II} \le I_c \tag{5}$$

$$M_r = \frac{1.5 f_{ct} I_c}{y_t} \tag{6}$$

By applying Equations 2 and 3 it is possible to obtain the moment-rotation curves over the entire monotonic loading history [15], which results in Figure 14a to Figure 14c for the twenty-seven models analyzed.

Figure 14a shows the moment-rotation curves for the nine models using Q345 steel with f_y = 436 MPa. It can be seen that, until the bolts begin to yield, the strength of the concrete has little influence on the stiffness of the connections. However, at higher values of connection rotation, after the bolts have yielded, the strength of the concrete becomes a more significant factor. Links with higher strength concrete have a higher bending moment resistance after the bolts have yielded.

Figure 14b shows the results of the nine models using CA-70 steel with f_y = 700 MPa. The conclusions are similar to those of the models using C385 steel with regard to the influence of concrete. However, it is noteworthy that in the models with a bolt diameter of 28 mm, soon after the first bolt in the connection yielded, the beam failed, characterized by yielding of the longitudinal reinforcement. This phenomenon limited the connection's ability to resist greater bending moments after the beam's longitudinal reinforcement had yielded.

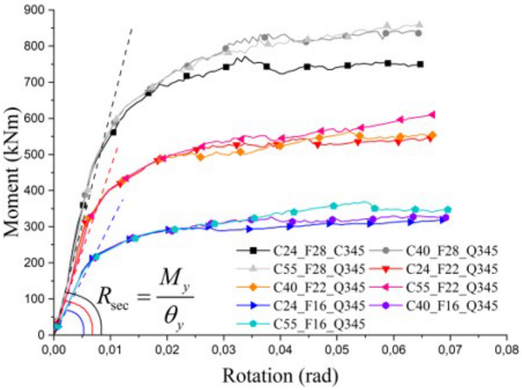

(a) Models reinforced with Q345 steel.

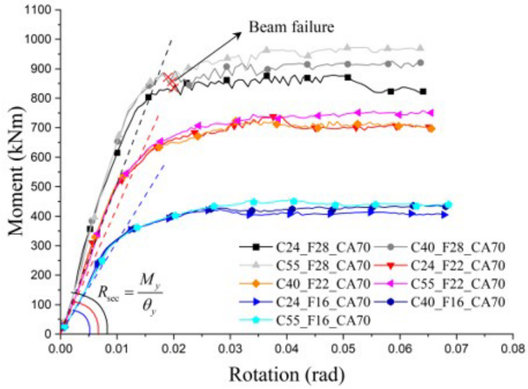

(b) Models reinforced with CA-70 steel.

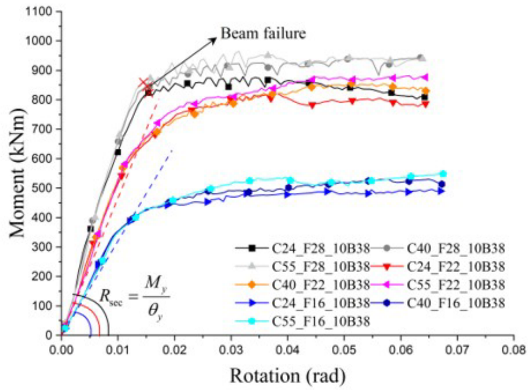

(c) Models reinforced with 10B38 high-strength steel.

Figure 14 . Moment-rotation curves for all simulated beam-to-column connection models using different steel types.

In turn, Figure 14c shows the results of the models with high strength 10B38 steel (Class 8.8), with f_y = 834 MPa. Similarly, the models with a 28 mm bolted diameter showed failure in the beam, characterized by yielding of the longitudinal reinforcement with subsequent crushing of the concrete at the end of loading. In this case, the beam failure occurred before the connection bolts had yielded. As a result, the secant stiffness of the connection was not calculated, and these results were omitted from the values presented in Table 5.

The secant stiffness of the connection was defined by the ratio between the bending moment resisted by the connection and its respective rotation when the first row of bolts in the connection located near the top face yielded. In the numerical modeling, the yield strength (P_y) was determined in the increment immediately after the nodal stresses in the bolts exceeded the yield strength of the steel (f_y) .

Figure 15 shows the values of secant stiffness (R_{sec}) as a function of bolt diameter (ϕ) for the connections analyzed. For the bottom diameters, associated with the 16 mm and 22 mm bolts, it can be seen that the secant stiffness is not very sensitive to the strength of the concrete or the type of steel used. In this range, the stiffness has been shown to be more dependent on the area of steel present in the connection, reflecting a direct influence of the bolt diameter on the behavior.

For the 28 mm bolts, the secant stiffness showed greater variability. The highest values were obtained with the lowest strength steel (Q345), suggesting that combining high reinforcement ratios with high strength steels can intensify concrete degradation, resulting in reduced bond stiffness.

Multiple linear regression analysis confirmed these results. The model was statistically significant [$F(3,23) = 112.28$; $p < 0.001$], explaining 94.4% of the variability in secant stiffness ($R^2 = 0.944$). Among the independent variables evaluated, only the diameter of the bolts showed statistical significance ($\beta = 0.946$; $t = 17.53$; $p < 0.001$). The strength of the concrete ($\beta = 0.007$; $t = -0.138$; $p = 0.891$) and the strength of the steel ($\beta = -0.101$; $t = -1.879$; $p = 0.075$) were not significant, indicating that, in isolation, they do not influence the variation in drying stiffness observed.

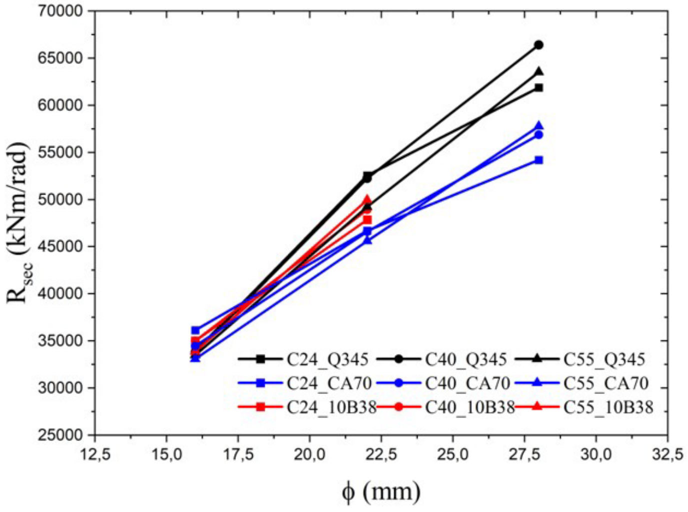

Figure 15. Relationship between secant stiffness and bolt diameter.

4.4 ANALYTICAL MODEL

Ferreira et al. [26] proposed an analytical model for calculating the secant stiffness of beam-column connections in precast structures. This analytical model was applied to the computationally analyzed models to assess their suitability for the bolted typology. Figure 16a shows the bolted typology, where the bolt positions and the lengths of interest, such as the width of the corbel (l_p) , the width of the corbel (l_c) and the plastic hinge length (l_{rp}) are illustrated.

Figure 16b illustrates the equilibrium of the cross-section for calculating the yield bending moment of the connection, according to Equation 7 . As an approximation, it has been assumed that the lever arm (z) is equal to $0.9d_1$, so Equations 8 to can be used to calculate the portion of bending moment resisted by each bolt line of the connection.

$$M_y = M_1 + M_2 + M_3 + M_4 \tag{7}$$

$$M_1 = 0.9 A_1 f_y d_1 \tag{8}$$

$$M_2 = \frac{A_2 f_y \left(0.9d_1 - \Delta_2\right)^2}{0.9d_1} \tag{9}$$

$$M_3 = \frac{A_3 f_y \left(0.9d_1 - 2\Delta_2\right)^2}{0.9d_1} \tag{10}$$

$$M_4 = \frac{A_4 f_y \left(0.9d_1 - 3\Delta_2\right)^2}{0.9d_1} \tag{11}$$

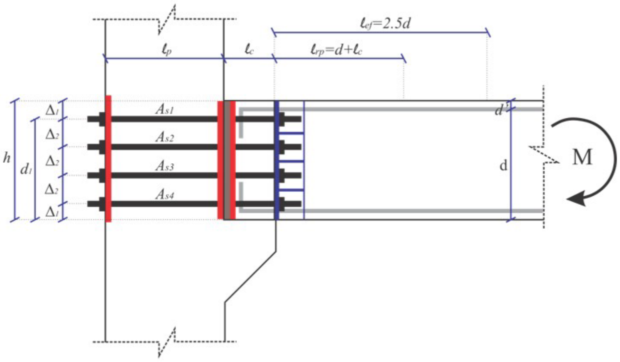

(a) Simplified schematic used to calculate the secant stiffness of the connection.

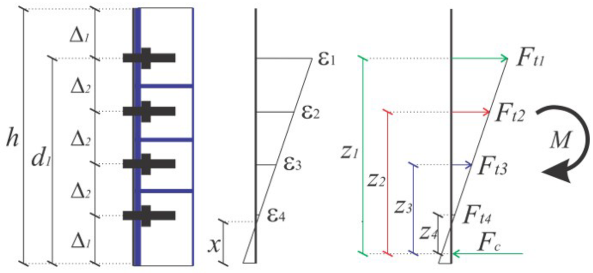

(b) Design section used for moment equilibrium analysis.

Figure 16. Analytical model and internal force distribution for the beam-to-column connection.

According to Ferreira et al. [26] the rotation in the connection region can be calculated using Equation 12, using β equal to unity. In this expression, the first portion corresponds to the opening of the joint between the faces of the beam and the column, resulting from the strain of the bolts, and the second accounts for the rotation due to the curvature of the beam in the connection region. The variables l_p, l_c and l_{rp} are shown in Figure 16a; f_y is the yield strength of the steel and E_s is the modulus of elasticity of the bolt steel, while d_1 is the effective depth of the connection. In the second plot, M_y is calculated from Equation 7, E_c is the modulus of elasticity of the concrete and I_{cr} is the critical inertia of the section, calculated from Equation 7 for the yield moment (M_y) .

$$\theta_y = \beta\left[\frac{f_y\left(l_p + l_c\right)}{E_s d_1} + \frac{M_y l_{rp}}{E_c I_{cr}}\right] \tag{12}$$

The joint rotation can be calculated using the simplified expression proposed in Equation 13. This equation is derived from the assumption that joint yielding is governed by the yielding of the first row of bolts. Concurrently, the longitudinal beam reinforcement is subjected to an average strain, ε_s, distributed over a cracked length equivalent to the plastic hinge region.

$$\theta_y = \frac{f_y\left(l_p + l_c\right)}{E_s d_1} + \frac{\varepsilon_s l_{ef}}{d} \tag{13}$$

$$\varepsilon_s = \frac{M_y}{0.9d\, A_s E_s} \tag{14}$$

$$l_{ef} = 2.5d \tag{15}$$

The first term of Equation 13 represents the rotational component attributed to bolt deformation. This is expressed as the bolt's yield strain (ε_y), multiplied by the combined length of the column width (l_p) and the widened beam end (l_c).

The second term of Equation 13 accounts for the rotation from the plastic hinge, which forms in the connection region characterized by a concentration of flexural cracking. The length of flexural cracking is typically estimated to be between 1.5 and 2.0 times the beam height [27]. The average strain in the beam's longitudinal steel reinforcement (ε_s) is determined using Equation 14. This strain is averaged over the cracked region, which was numerically verified to be approximately 2.5 times the effective depth of the beam, as shown in Equation 15 and Figure 17. This value is consistent with the observations of Coelho and Araújo [15], who investigated a beam-column connection with continuous reinforcement ratios ranging from 1.4% to 2.8%. This assumption leads to the formulation of the second term, thereby completing the derivation of Equation 13.

Table 5 shows the results of the application and comparison of the analytical models with the numerical results obtained in the parametric analysis.

Table 5. Calculation of secant stiffness from analytical models.

Model	$R_{sec,Ana}$ [kN·m/rad] β = 1.0	$R_{sec,Ana}$ [kN·m/rad] β = 0.8	$R_{sec,Ana}$ [kN·m/rad] proposed	$R_{sec,Num}$ [kN·m/rad]	$R_{sec,Num}/R_{sec,Ana}$ β = 1.0	$R_{sec,Num}/R_{sec,Ana}$ β = 0.8	$R_{sec,Num}/R_{sec,Ana}$ proposed
C24_F28_Q345	76256	61004.6	61392	61894.2	0.81	1.01	1.01
C40_F28_Q345	80718	64574.7	61392	66416.8	0.82	1.03	1.08
C55_F28_Q345	86387	69109.8	61392	63515.1	0.74	0.92	1.03
C24_F22_Q345	61089	48871.1	49251	52552.0	0.86	1.08	1.07
C40_F22_Q345	68038	54430.6	49251	52237.0	0.77	0.96	1.06
C55_F22_Q345	74710	59767.8	49251	49236.1	0.66	0.82	1.00
C24_F16_Q345	43487	34789.9	33727	33902.1	0.78	0.97	1.01
C40_F16_Q345	45833	36666.3	33727	33775.0	0.74	0.92	1.00
C55_F16_Q345	46256	37004.4	33727	33497.8	0.72	0.91	0.99
C24_F28_CA-70	73053	58442.5	59604	54188.8	0.74	0.93	0.91
C40_F28_CA-70	74834	59867.1	59604	56876.5	0.76	0.95	0.95
C55_F28_CA-70	76804	61443.2	59604	57772.3	0.75	0.94	0.97
C24_F22_CA-70	56827	45461.5	47817	46690.0	0.82	1.03	0.98
C40_F22_CA-70	59439	47551.5	47817	46582.7	0.78	0.98	0.97
C55_F22_CA-70	62649	50119.1	47817	45599.6	0.73	0.91	0.95
C24_F16_CA-70	38621	30896.4	32745	36134.7	0.94	1.17	1.10
C40_F16_CA-70	41923	33538.5	32745	34466.5	0.82	1.03	1.05
C55_F16_CA-70	44312	35449.7	32745	33101.0	0.75	0.93	1.01
C24_F28_10B38	-	-	-	-	-	-	-
C40_F28_10B38	-	-	-	-	-	-	-
C55_F28_10B38	-	-	-	-	-	-	-
C24_F22_10B38	59075	47260.2	50207	47848.3	0.81	1.01	0.95
C40_F22_10B38	60910	48728.2	50207	48916.6	0.80	1.00	0.97
C55_F22_10B38	63150	50520.0	50207	49960.6	0.79	0.99	1.00
C24_F16_10B38	39539	31631.0	34382	34994.8	0.89	1.11	1.02
C40_F16_10B38	42218	33774.1	34382	34997.0	0.83	1.04	1.02
C55_F16_10B38	44646	35716.7	34382	33864.0	0.76	0.95	0.98
			Average		0.79	0.98	1.00
			Standard Deviation		0.059	0.074	0.046
			COV (%)		7.49	7.49	4.54

The stiffness results obtained directly from the model by Ferreira et al. [26] using $\beta = 1$ were overestimated for this typology, resulting in an average $R_{sec,num}/R_{sec,ana}$ ratio 0.79. To correct this discrepancy, a new coefficient was proposed, $\beta = 0.8$, which resulted in an $R_{sec,num}/R_{sec,ana}$ ratio 0.98, while maintaining low values for standard deviation (0.074) and coefficient of variation (COV = 7.49%).

On the other hand, when using the simplified Equation to calculate the rotations, the analytical model showed a better fit, achieving an $R_{sec,num}/R_{sec,ana}$ ratio 1 and a COV of only 4.54%. These results demonstrate the good performance of analytical modeling in predicting the secant stiffness of this type of connection.

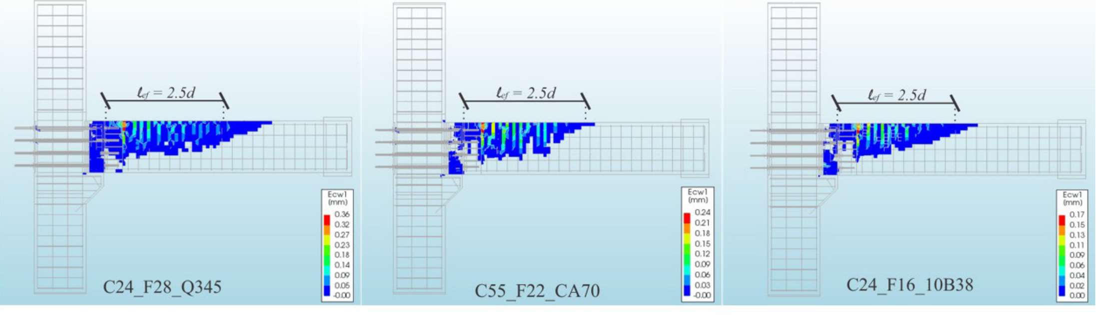

Figure 17. Effective strain length of the beam's longitudinal reinforcement from the flow of bending cracks.

5 CONCLUSIONS

The numerical model developed in DIANA® accurately represented the behavior of the bolted beam-column connection, with a maximum error of 3% in the estimation of the ultimate resistance and 30% in energy dissipation. In addition, it adequately captured the cracking pattern, stiffness and global behavior of the connection, validating the constitutive models adopted for the materials and interfaces.

The comparison between the loading regimes indicated low sensitivity of the connection to the type of stress before the yielding of the first row of bolts. The strength and stiffness curves have been shown to behave similarly between the models subjected to monotonic and cyclic loading

The parametric analysis with monotonic loading indicated that the secant stiffness of the connection, determined at bolt yielding, is little influenced by the strength of the concrete and the type of steel, being more sensitive to the steel area of the bolts. Connections using bolts with lower yield strength exhibited the highest secant stiffness, likely due to reduced concrete degradation, as the use of high-strength bolts caused greater deterioration of the concrete in the connection.

In the analytical modeling, the model by Ferreira et al. [26] overestimated the stiffness of the bolted connection. To correct this discrepancy, an adjustment coefficient of $\beta = 0.8$ was proposed, resulting in a ratio of $R_{sec,num}/R_{sec,ana} = 0.98$ and a coefficient of variation of only 7.49%. When used the simplified equation to calculate the rotation of the link, $R_{sec,num}/R_{sec,ana} = 1.00$ was obtained, with a coefficient variation of only 4.54%.

The results obtained strengthen the efficiency of the numerical modeling carried out and the feasibility of the analytical model adjusted to predict the secant stiffness of this type of beam-column connection. These findings contribute to improving the design of semirigid connections in precast structures, helping to define more efficient criteria for their design.

ACKNOWLEDGEMENTS

The authors would like to thank the Coordenação de Aperfeiçoamento de Pessoal de Nível Superior – Brasil (CAPES) – Finance Code 001; and the National Council for Scientific and Technological Development (CNPq) [grant number 305622/2023-4] for financing this research.

REFERENCES

[1] Y. Bao and K. H. Tan, "Experimental and numerical study on performance of precast concrete wet and dry joints under progressive collapse scenario," *J. Build. Eng.*, vol. 74, pp. 106739, 2023, https://doi.org/10.1016/j.jobe.2023.106739.

[2] Y. C. Kurama et al., "Seismic-resistant precast concrete structures: state of the art," *J. Struct. Eng.*, vol. 144, no. 4, pp. 03118001, 2018, https://doi.org/10.1061/(ASCE)ST.1943-541X.0001972.

[3] M. E. Rodríguez and M. Torres-Matos, "Seismic behavior of a type of welded precast concrete beam-column connection," *PCI J.*, vol. 58, no. 3, pp. 81–94, 2013, https://doi.org/10.15554/pcij.06012013.81.94.

[4] International Federation for Structural Concrete, *Seismic Design of Precast Concrete Building Structures. State-of-Art Report Prepared by Task Group 7.3* (Bulletin 27). Lausanne: FIB, 2003.

[5] W. Xue and X. Yang, "Seismic tests of precast concrete, moment resisting frames and connections," *PCI J.*, vol. 55, no. 3, pp. 102–121, 2010, https://doi.org/10.15554/pcij.06012010.102.121.

[6] S. M. Alcocer, R. Carranza, D. Perez-Navarrete, and R. Martinez, "Seismic tests of beam-to-column connections in a precast concrete frame," *PCI J.*, vol. 47, no. 3, pp. 70–89, 2002, https://doi.org/10.15554/pcij.05012002.70.89.

[7] M.-S. Jo, H.-G. Kim, D.-H. Kim, Y.-J. Lee, S.-P. Han, and K.-H. Kim, "Emulation evaluation of interior beam – column connections in PC and RC moment-resisting frames," *Materials*, vol. 16, no. 21, pp. 6906, 2023.

[8] American Concrete Institute, *Guide for Testing Reinforced Concrete Structural Elements under Slowly Applied Simulated Seismic Loads*, ACI 374.2R-13, 2013.

[9] D. Guan, C. Jiang, Z. Guo, and H. Ge, "Development and seismic behavior of precast concrete beam-to-column connections," *J. Earthquake Eng.*, vol. 22, no. 2, pp. 234–256, 2018, https://doi.org/10.1080/13632469.2016.1217807.

[10] P. K. Aninthaneni, R. P. Dhakal, J. Marshall, and J. Bothara, "Nonlinear cyclic behaviour of precast concrete frame sub-assemblies with 'dry' end plate connection," *Structures*, vol. 14, pp. 124–136, 2018, https://doi.org/10.1016/j.istruc.2018.03.003.

[11] P. K. Aninthaneni, R. P. Dhakal, J. Marshall, and J. Bothara, "Experimental investigation of 'dry' jointed precast concrete frame sub-assemblies with steel angle and tube connections," *Bull. Earthquake Eng.*, vol. 18, no. 8, pp. 3659–3681, 2020, https://doi.org/10.1007/s10518-020-00837-9.

[12] P. K. Aninthaneni and R. P. Dhakal, "Analytical and numerical investigation of 'dry' jointed precast concrete frame sub-assemblies with steel angle and tube connections," *Bull. Earthquake Eng.*, vol. 17, no. 9, pp. 4961–4985, 2019, https://doi.org/10.1007/s10518-019-00663-8.

[13] R. Zhang, Y. Zhang, A. Li, and T. Y. Yang, "Experimental study on a new type of precast beam-column joint," *J. Build. Eng.*, vol. 51, pp. 104252, 2022, https://doi.org/10.1016/j.jobe.2022.104252.

[14] J. Liu, Y. Liu, and D. Yu, "Experimental and numerical studies on the seismic performance of new assembled concrete frame beam–column joints," *Buildings*, vol. 13, no. 2, pp. 329, 2023, https://doi.org/10.3390/buildings13020329.

[15] S. A. Coelho and D. L. Araújo, "Nonlinear finite element model of the beam to column connection for precast concrete frames with high ratio of the continuity tie bars," *Comput. Concr.*, vol. 31, no. 1, pp. 53–69, 2023, https://doi.org/10.12989/cac.2023.31.1.053.

[16] S. Kallam and S. B. K. Borghate, "Nonlinear numerical evaluation of dry precast beam column connection with embedded bolts," *Lat. Am. J. Solids Struct.*, vol. 19, no. 7, pp. 1–18, 2022, https://doi.org/10.1590/1679-78257314.

[17] T. T. Ngo, T. M. Pham, H. Hao, W. Chen, and N. S. Ha, "Proposed new dry and hybrid concrete joints with GFRP bolts and GFRP reinforcement under cyclic loading: testing and analysis," *J. Build. Eng.*, vol. 49, pp. 104033, 2022, https://doi.org/10.1016/j.jobe.2022.104033.

[18] J. D. Nzabonimpa, W.-K. Hong, and S.-C. Park, "Experimental investigation of dry mechanical beam-column joints for precast concrete based frames," *Struct. Des. Tall Spec. Build.*, vol. 26, no. 1, e1302, 2017, https://doi.org/10.1002/tal.1302.

[19] K. Maekawa and N. Fukuura, "Nonlinear modeling of 3D structural reinforced concrete and seismic performance assessment," in *Infrastructure Systems for Nuclear Energy*, T. T. C. Hsu, C.-L. Wu and J.-L. Li, Eds., New York: Wiley, 2013, pp. 153–184, http://dx.doi.org/10.1002/9781118536254.ch11.

[20] J. C. Lim and T. Ozbakkaloglu, "Stress-strain model for normal- and light-weight concretes under uniaxial and triaxial compression," *Constr. Build. Mater.*, vol. 71, pp. 492–509, 2014, https://doi.org/10.1016/j.conbuildmat.2014.08.050.

[21] Fédération Internationale du Béton, *Model Code for Concrete Structures 2010*, 1st ed. Berlin: Ernst & Sohn, 2013.

[22] International Federation for Structural Concrete, *fib Model Code for Concrete Structures 2020*. Lausanne: FIB, 2021, 646 pp.

[23] V. Kodur, M. Yahyai, A. Rezaeian, M. Eslami, and A. Poormohamadi, "Residual mechanical properties of high strength steel bolts subjected to heating-cooling cycle," *J. Construct. Steel Res.*, vol. 131, pp. 122–131, 2017, https://doi.org/10.1016/j.jcsr.2017.01.007.

[24] A. F. Shaikh and D. E. Branson, "Non-tensioned steel in prestressed concrete beams," *PCI J.*, vol. 15, no. 1, pp. 14–36, 1970, https://doi.org/10.15554/pcij.02011970.14.36.

[25] Associação Brasileira de Normas Técnicas, *Projeto de Estruturas de Concreto*, ABNT NBR 6118, 2023.

[26] M. A. Ferreira, M. K. El Debs, and K. S. Elliott, "Modelo teórico para projeto de ligações semi-rígidas em estruturas de concreto pré-moldado," in *An. 44° Congr. Bras. Concr.*, no. 1, 2002, pp. 1–16.

[27] Fédération Internationale du Béton. *Structural Connections for Precast Concrete Buildings: Guide to Good Practice Prepared by Task Group 6.2* (Bulletin 43), 1st ed. Cham: Int. Fed. Struct. Concr., 2008.

Author contributions: Contribution description of each co-author for the study. YMN: modeling, analysis, writing; DLA: formal analysis, review; MAF: revision.

Editors: José Marcio Calixto, Daniel Cardoso.